



**HAL**  
open science

# Numerical Simulations of High Prandtl Number liquid jets Impinging on a Flat Plate

Adèle Poubeau, Guillaume Vinay, Bidzina Kekelia, Kevin Bennion

► **To cite this version:**

Adèle Poubeau, Guillaume Vinay, Bidzina Kekelia, Kevin Bennion. Numerical Simulations of High Prandtl Number liquid jets Impinging on a Flat Plate. *International Journal of Heat and Mass Transfer*, 2023, 205, pp.123889. 10.1016/j.ijheatmasstransfer.2023.123889 . hal-04056791

**HAL Id: hal-04056791**

**<https://ifp.hal.science/hal-04056791v1>**

Submitted on 3 Apr 2023

**HAL** is a multi-disciplinary open access archive for the deposit and dissemination of scientific research documents, whether they are published or not. The documents may come from teaching and research institutions in France or abroad, or from public or private research centers.

L'archive ouverte pluridisciplinaire **HAL**, est destinée au dépôt et à la diffusion de documents scientifiques de niveau recherche, publiés ou non, émanant des établissements d'enseignement et de recherche français ou étrangers, des laboratoires publics ou privés.

# Numerical simulations of high Prandtl number liquid jets impinging on a flat plate

Adèle Poubeau<sup>a,\*</sup>, Guillaume Vinay<sup>a</sup>, Bidzina Kekelia<sup>b</sup>, Kevin Bennion<sup>b</sup>

<sup>a</sup>*IFP Energies nouvelles, Institut Carnot IFPEN Transports Energie, 1 et 4 avenue de Bois-Préau, Rueil-Malmaison, 92500, France*

<sup>b</sup>*National Renewable Energy Laboratory, 15013 Denver West Parkway, Golden, CO 80401, USA*

---

## Abstract

In this work, 3D simulations of oil jets impinging on a flat, heated wall are presented. The numerical setup uses the Volume of Fluid (VoF) method to model the two-phase flow. A careful grid definition across the liquid film, along with the use of the Conjugate Heat Transfer (CHT) approach allowed local heat transfer to be solved with fine resolution at the wall. Variations of liquid flow rate, liquid temperature and surface temperature allow to cover a wide range of local Reynolds and Prandtl numbers ( $226 < Re < 2850$ ,  $77 < Pr < 161$ ). Resulting surface-averaged heat transfer compares very well with experimental measurements conducted in a previous study. In-depth analysis of the flow has identified expected features from the literature. In particular, the impact of jet axial velocity profiles on the heat transfer distribution in the stagnation zone was clearly stated. The increase in heat transfer when warming the liquid film was also reproduced and explained by a decrease in oil viscosity and an increase in film velocity. All those effects

---

\*Corresponding author

*Email address:* `adele.poubeau@ifpen.fr` (Adèle Poubeau)

were taken into account in correlations for stagnation and local values of Nusselt number. A grid sensitivity study was also conducted, showing that if the grid solving the thermal boundary layer in the stagnation zone can be coarsened without impacting local and surface-averaged predictions of heat transfer, a minimum resolution (2 to 3 cells) within the thermal boundary layer is however required for an accurate prediction of heat transfer.

*Keywords:* conjugate heat transfer, volume of fluid, high Prandtl number, liquid jet impingement, electric machine cooling

---

## Nomenclature

$\bar{f}$	surface average of variable $f$ , $\bar{f} = \frac{1}{A} \int_A f dA$
$\dot{m}$	mass flow rate [ $\text{kg} \cdot \text{s}^{-1}$ ]
$\dot{q}$	heat flux [ $\text{W} \cdot \text{m}^{-2}$ ]
$\dot{v}$	volumetric flow rate [ $\text{l} \cdot \text{min}^{-1}$ ]
$A$	target surface area, $A = \pi R^2$
$B$	Dimensionless radial velocity gradient
$c_p$	heat capacity [ $\text{J} \cdot \text{kg}^{-1} \text{K}^{-1}$ ]
$D$	target diameter [m]
$d$	nozzle orifice diameter [m]
$d_1$	distance between the two thermocouples embedded in the target [m]
$d_2$	distance between the cooled surface and the upper thermocouple [m]
$f(r, z)$	radial profile of variable $f$ , $f(r, z) = \frac{1}{2\pi} \int_0^{2\pi} f(r, \theta, z) d\theta$

$H$	distance nozzle exit to wall [m]
$h$	heat transfer coefficient [ $\text{W} \cdot \text{m}^{-2} \cdot \text{K}^{-1}$ ]
$H_{film}$	film thickness [m]
$k$	thermal conductivity [ $\text{W} \cdot \text{m}^{-1} \cdot \text{K}^{-1}$ ]
$l$	nozzle length [m]
$Nu$	Nusselt number
$Nu_0$	Nusselt number in the stagnation zone
$Pr$	Prandtl number
$q$	heat transfer rate, $q = \int_A \dot{q} dA$ [ $\text{J} \cdot \text{s}^{-1}$ ]
$R$	target radius [m]
$r, \theta, z$	cylindrical coordinates, $r = \sqrt{x^2 + y^2}$
$r_1$	radial extension of the stagnation zone [m]
$r_2$	radial extension of the boundary layer zone [m]
$Re$	Reynolds number
$T_f$	nozzle inlet fluid temperature [K]
$T_s$	average surface temperature [K]
$T_{aw}$	Adiabatic wall temperature [K]
$u_f$	liquid jet bulk velocity [ $\text{m} \cdot \text{s}^{-1}$ ]
$u_r$	radial velocity [ $\text{m} \cdot \text{s}^{-1}$ ]
$x, y, z$	cartesian coordinates

### **Greek symbols**

$\Delta$	cell size [m]
$\delta$	hydrodynamic boundary layer thickness [m], $u_r(r, \delta(r)) = 0.99 \max_z u_r(r, z)$
$\delta_t$	thermal boundary layer thickness [m], $T(r, \delta_t(r)) = T_s(r) + 0.99(T_f - T_s(r))$
$\Delta_x, \Delta_y, \Delta_z$	cell size in the directions $x, y, z$ [m]
$\mu$	dynamic viscosity [ $\text{N} \cdot \text{s} \cdot \text{m}^{-2}$ ]
$\nu$	kinematic viscosity [ $\text{m}^2 \cdot \text{s}^{-1}$ ]
$\rho$	density [ $\text{kg} \cdot \text{m}^{-3}$ ]
$\sigma$	surface tension [ $\text{N} \cdot \text{m}^{-1}$ ]

### Subscripts

$f$	fluid
$j$	jet
$s$	surface

## 1. Introduction

Thermal management is crucial for electric machines. Increasing power density while ensuring the integrity of components such as magnets and windings, which can be irreversibly degraded by excessive temperature increase, encourages the use of various strategies for their effective cooling. Those solutions can be passive (via the design and the choice of materials, like laminated steel foils to reduce magnetic losses) or active (forced convection by air or water jacket). They can be combined with direct oil cooling of active components (such as end-windings, slot-windings and/or rotor) by jet,

spray or dripping, creating a cooling liquid film. This approach, allowing high heat flux removal, is considered today as promising [1, 2, 3]. However, direct cooling with oil requires finding a compromise between cooling efficiency, powertrain integration and cost. There is a clear need for experimental and numerical studies to provide further understanding of the complex phenomena at stake and validate methods for prediction of cooling performance in electric machines. Numerically, modeling direct oil cooling of electric machines remains challenging: the liquid phase is destabilized by a crossflow of air due to rotor movement and interacts with a complex surface (traditional or hairpin windings) by splashing or forming films, all this in a multi-scale context. Correctly predicting heat transfer requires accounting for all these aspects. High-fidelity approach such as Volume of Fluid (VoF) in 3D Computational Fluid Dynamics (CFD) represents an interesting tool for its ability to model complex, unsteady two-phase flows along with heat transfer characterization. In this context, the present study focuses on oil jet cooling, a reliable and easy-to-implement technique, with lower pump losses compared to spray cooling. There is a wide literature regarding free-surface liquid jet impingement, with experimental studies [4, 5, 6, 7, 8, 9], theoretical analysis [10, 11, 12, 13, 14, 15] or simulations [16, 17, 18]. Those studies described the particular flow structure of laminar or turbulent impinging jets and characterized local heat transfer (notably the dependency in Reynolds ( $Re$ ) and Prandtl numbers ( $Pr$ )) and investigated various effects, like the nozzle geometry or the nozzle-to-wall distance. However, most of those studies considered fluids with relatively low  $Pr$ , while with oil as the cooling fluid, Prandtl number can exceed 300, depending on the temperature. A few ex-

perimental studies focused on high Prandtl number liquid jets, characterizing surface-averaged heat transfer [19, 20, 21] or local heat transfer [22, 23, 24]. To the best of our knowledge, numerical studies of impinging jets for high  $Pr$  fluids are very limited [25, 26] and tend to validate their numerical approach on low  $Pr$  cases, by a comparison to correlations from the literature.

The objective of the present study is to perform and validate fully resolved 3D simulations of Automatic Transmission Fluid (ATF) jet impinging on a heated flat plate, using the VoF method for an accurate modeling of the two-phase flow, and the Conjugate Heat Transfer (CHT) approach to predict heat transfer at the wall. Particular attention was paid to the grid definition in the film, in order to resolve the thermal boundary layer, which is especially thin due to the high Prandtl numbers. The operating conditions are those of the experiments performed in [21], which characterized surface-averaged heat transfer for a wide range of Reynolds and Prandtl numbers, as well as a variation of surface temperature. This particular experimental setup offers the advantage of having a limited radial extension of the heated solid: the computational domain remains small, which keeps the computational cost small as well, and allows a wide range of effects to be numerically evaluated and studied (liquid flow rate, liquid jet temperature and surface heat flux). After a description of the experimental and numerical setups, the surface-averaged Nusselt numbers obtained numerically and experimentally are compared. Then, a detailed analysis of the jet and flow along the impinging wall is presented, comparing numerical results with the knowledge in the literature. Heat transfer is also characterized, and Nusselt number correlations are derived with the only objective to further validate the numerical

model (the short radial domain limits their application). Finally, with the objective to adapt this numerical approach to future simulations of cooling of a full-scale electric machine, for which grid cell size will be critical, a grid sensitivity study is performed to evaluate the impact of the grid resolution within the liquid film on the local and average heat transfer.

## 2. Experimental setup

The experimental setup is illustrated in Fig. 1 and fully detailed in [21]. An orifice nozzle of diameter  $d = 2.06 \text{ mm}$  is positioned perpendicularly to a heated target assembly, at a fixed distance  $H = 10 \text{ mm}$ . The liquid volumetric flow rate  $\dot{v}$  and liquid temperature at the nozzle inlet  $T_f$  can be finely controlled and measured. The target assembly is a cylinder of diameter  $D = 12.7 \text{ mm}$ , made of oxygen-free copper. A resistance heater is installed on the bottom, delivering a heat flux  $\dot{q}$ , and a housing ensures a thermal insulation on the sides. Two K-type thermo-couples, denoted TC1 and TC2, are embedded at different heights in the target (see Fig.1b). Due to the high thermal conductivity  $k$  of the copper target and the low conductivity of the housing, one-dimensional heat transfer within the target can be assumed. In steady-state conditions, heat flux  $\dot{q}$  can be calculated as:

$$\dot{q} = -k \frac{T_{TC1} - T_{TC2}}{d_1} \quad (1)$$

and

$$\dot{q} = -k \frac{T_s - T_{TC1}}{d_2} \quad (2)$$

where  $T_s$  is the target surface temperature. From the above equations, the later can be expressed as:

$$T_s = T_{TC1} + (T_{TC1} - T_{TC2})\frac{d_2}{d_1} \quad (3)$$

Then, the surface-averaged heat transfer coefficient  $\bar{h}$  is calculated as follows:

$$\bar{h} = \frac{\dot{q}}{T_s - T_f} = k \frac{T_{TC2} - T_{TC1}}{d_1(T_{TC1} - T_{Tf}) - d_2 T_{TC2} - T_{TC1}} \quad (4)$$

Measurements were performed for various fluid temperatures  $T_f$ , flow rate  $\dot{v}$  and target surface temperature  $T_s$  (via a control of the resistance heater, varying the heat flux  $\dot{q}$ ). For the simulation, a subset of these variations was considered (20 cases in total), described in Table 1. Impinging jets are usually characterized by their Reynolds number ( $Re$ ), based on the jet bulk velocity  $u_f$  and the nozzle diameter  $d$ . Here, the bulk velocity is estimated from the fluid mass flow rate  $\dot{m}$ :

$$Re = \frac{u_f d}{\nu_f} = \frac{4\dot{m}}{\pi \mu_f d} \quad (5)$$

The Prandtl number, the ratio of momentum diffusivity to thermal diffusivity, is defined as follows:

$$Pr = \frac{c_{p,f} \mu_f}{k_f} \quad (6)$$

where  $c_{p,f}$  and  $k_f$  are the heat capacity and the thermal conductivity, respectively, of the liquid. As liquid properties, and in particular the viscosity, vary strongly with temperature, both Reynolds and Prandtl numbers are evaluated at the local film temperature  $(T_f + T_s)/2$  (considering  $T_s$  uniform over the target). To facilitate the comparison to other studies, a jet Reynolds number  $Re_j$  is also considered, following the same definition as Eq. 5, but

evaluating the viscosity at  $T = T_f$ . Considering the parametric variations listed in Table 1,  $Re$  ranges between 226 and 2850, and  $Pr$  between 77 and 161. The jet Reynolds number  $Re_j$  does not exceed 2000.

### 3. Numerical setup

#### 3.1. Computational domain

One of the objectives of the present study is to validate a CHT approach for future simulations of liquid cooling of electric machines. Consequently, even if the surface temperature  $T_s$  of the solid target can reasonably be assumed uniform, the target was nonetheless included in the computational domain to solve the CHT problem. The computational domain is represented in Fig. 2, with the upper, fluid part (with ambient air, cooling liquid jet and the subsequent film) and the lower, solid part (the heated target assembly). It extends radially up to  $r = R$ , the target radius. The fluid domain includes the nozzle of  $l = 3\text{ mm}$  length. The nozzle exit is located at a distance  $H$  from the impinged wall. A uniform mass flow rate  $\dot{m}$  of liquid is imposed at the nozzle inlet, and a no-slip, adiabatic boundary condition is imposed on the nozzle wall. An outlet boundary condition is imposed at  $r = R$ . The interface between fluid and solid domains is represented in dark grey. A no-slip condition is imposed on the fluid side. The target assembly itself is modelled by a pure copper solid and is heated by a uniform heat flux  $\dot{q}$  imposed at the bottom. An adiabatic condition is imposed on the side. For reference, the location of the two thermo-couples used in the experiments are noted in Fig. 2. The jet impinging point is located at  $(x, y, z) = (0, 0, 0)$ . As the jet impinges at the center of the target, only a quarter of the geometry

was computed, with symmetric boundary conditions applied to the  $x$  and  $y$  directions.

The properties of the liquid and solid are listed in Table 2. Viscosity, heat capacity and thermal conductivity were provided by the ATF manufacturer<sup>1</sup>. The surface tension was estimated from a typical ATF [27]. Solid properties are those of pure copper.

### 3.2. Grid definition

The grid imposed in both fluid and solid computational domains is shown in Fig. 2. A fixed grid of cell size  $62.5 \mu m$  is imposed in the nozzle and in the liquid jet region (including the interface liquid/air). In the nozzle, 6 layers of refined cells ( $31 \mu m$ ) are imposed along the wall, with a first cell height of  $10 \mu m$ , to ensure the resolution of the viscous boundary layer. After impingement, the film region and the interface liquid/air is captured by a boundary-layer grid, with  $\Delta_x = \Delta_y = 100 \mu m$ , a minimum cell height at the wall  $\Delta_{z,min} = 3 \mu m$  and an expansion ratio of 1.04. This grid allows an excellent resolution of both viscous and thermal boundary layers for all cases simulated, and in particular of the most restrictive region in terms of grid resolution: the stagnation zone. In this region, the thermal boundary layer thickness  $\delta_{t,stagn}$  is minimal. An analytical approach in [28] correlates the viscous boundary layer thickness in the stagnation zone  $\delta_{stagn}$  with the nozzle diameter  $d$  and  $Re$ :

$$\delta_{stagn} \sim dRe^{-1/2} \quad (7)$$

---

<sup>1</sup>Ford Motor Company

Assuming  $\delta_t \sim \frac{\delta}{Pr^{1/3}}$  yields

$$\delta_{t, stagn} \sim dRe^{-1/2}Pr^{-1/3} \quad (8)$$

According to this formula, the most critical case (with the smallest  $\delta_{t, stagn}$ ) among the simulated variations corresponds to the case with the highest Reynolds number  $Re = 2850$  ( $T_f = 363 K$ ,  $T_s = 393 K$ ,  $\dot{v} = 1.5 l.min^{-1}$ ,  $Pr = 77$ ). This point was simulated first, and showed excellent predictions of heat transfer coefficient compared to the measurement, with an error of only 3% (within the experimental uncertainty), thus conforming the choice of the grid definition. For further validation, a sensitivity study on the boundary-layer grid, presented in Sec. 7, highlights how the grid resolution of the stagnation zone affects the average heat transfer over the entire surface. In the solid domain, the base cell size for the grid is  $\Delta = 0.5 mm$ . Along the interface with the fluid domain (where non-unidirectional effects are expected), a finer grid is imposed, with a minimum cell size  $\Delta_z = 13.75 \mu m$  at the interface, to limit interpolation error in the conjugated heat transfer resolution. The total number of cells is 350,000 for the fluid domain, and 90,000 for the solid domain.

### 3.3. Numerical methods

The two-phase flow is modelled by the VoF approach [29]. Both phases are considered incompressible and share a mass, momentum and energy equation. In particular, the momentum equation accounts for the gravitational acceleration and the surface tension effects:

$$\rho \left[ \frac{\partial u_i}{\partial t} + \frac{\partial(u_j u_i)}{\partial x_j} \right] = -\frac{\partial p}{\partial x_i} + \frac{\partial}{\partial x_j} \left[ \mu \left( \frac{\partial u_i}{\partial x_j} + \frac{\partial u_j}{\partial x_i} \right) \right] + \rho g_i + \sigma \kappa n_i \quad (9)$$

where  $g$  is the gravitational acceleration,  $\sigma$  the surface tension of the liquid,  $\kappa$  the curvature and  $\mathbf{n}$  the unit normal. In addition to the mass, momentum and energy, the volume fraction  $\alpha$  is also transported to describe the evolution of the free surface in time:

$$\frac{\partial \alpha}{\partial t} + u_j \frac{\partial \alpha}{\partial x_j} = 0 \quad (10)$$

The value of  $\alpha$  indicates the presence ( $\alpha = 1$ ) or absence ( $\alpha = 0$ ) of gas in the control volume. Finally, the following constitutive relations between material properties are considered:

$$\rho = \rho_1 \alpha + \rho_2 (1 - \alpha) \quad (11)$$

$$\mu = \mu_1 \alpha + \mu_2 (1 - \alpha) \quad (12)$$

where indices 1 and 2 represent the air and liquid properties, respectively. Equations 9-12 are solved in the finite-volume CFD code CONVERGE (v3.0.21). Considering the low values of Reynolds number encountered, no turbulence model was used. A pressure-based PISO algorithm (with a tolerance fixed at  $10^{-5}$ ) is applied, and pressure, momentum and energy terms are discretized with a second-order upwind scheme. To discretize the convective term in the transport equation of  $\alpha$  (Eq. 10), the High-Resolution Interface Capturing (HRIC) scheme is used [30]. Finally, as experimental heat transfer are characterized in steady-state condition, the steady-state solver is applied to limit computational time. A pseudo time-step is used, determined by the maximum convection CFL number, fixed at 1.5 for all cases.

All cases are solved as CHT simulations: at every time step of the fluid simulation, conduction is solved in the solid domain and thermal continuity

is imposed across the fluid/solid interface (continuity in heat flux and temperature). Typical time scales of thermal evolution in solids are much larger than fluid time scales, which can increase dramatically the simulation time. To accelerate the simulation, every 100 iterations, the fluid solver is paused, and only conduction in the solid is solved. At this point, the fluid/solid thermal coupling is replaced by a convective boundary condition, derived from the average of the last 100 iterations. After the convergence of the solid temperature, the CHT simulation is resumed.

### 3.4. Convergence of simulations

The flow aerodynamics converges rapidly, with a relative error between the inlet and outlet mass flow less than 0.005%. The thermal convergence, however, is longer to establish, as illustrated in Fig. 3 for the case  $T_f = 343 K$ ,  $T_s = 363 K$  and  $\dot{v} = 1.5 l.min^{-1}$ . Figure 3a shows that nearly 400,000 iterations are necessary for the total heat dissipation computed at the target surface  $q_s$  to converge towards the value  $q$  imposed at the bottom of the target. We consider the simulation to be converged when  $|q_s - q|/q$  is less than 0.2%. This criteria ensures a reasonably converged average surface temperature  $\overline{T}_s$ , as illustrated in Fig. 3b. The resulting return time is about 15 hours per case, on 2 nodes (4 CPUs Intel Skylake G-6140, 72 cores).

## 4. Comparison of the averaged heat transfer coefficients with experiments

In the cases considered, the jet velocity is low enough for the viscous dissipation to be negligible (see Appendix A). The local heat transfer coefficient

obtained by simulation is defined as

$$h(r) = \frac{\dot{q}(r)}{T_s(r) - T_f} \quad (13)$$

In the literature, heat transfer is mainly expressed using the dimensionless Nusselt number,  $Nu$ :

$$Nu(r) = \frac{h(r)d}{k_f} \quad (14)$$

The Nusselt number averaged over the target surface is then written

$$\overline{Nu} = \frac{\overline{\dot{q}}d}{k_f(\overline{T_s} - T_f)} \quad (15)$$

As the simulated surface temperature is almost uniform (with  $T_{s,max} - T_{s,min}$  less than 1 K),  $\overline{T_s}$  is denoted  $T_s$  in the rest of this manuscript, for the sake of simplicity. Figure 4 shows the comparison between experimental and simulated average Nusselt number  $\overline{Nu}$ . The CFD model compares very well to the measurements, with most of the numerical results being within the uncertainty range of the experimental values. This good agreement over the entire range of  $Re$  and  $Pr$  considered validates the numerical approach.

## 5. Physical analysis of high Prandtl, laminar jet impingement flow

### 5.1. Flow regions analysis

A free liquid jet impinging on a flat wall evolves into distinctive regions which have been identified and described analytically [10, 12, 28, 15] or experimentally [7, 31] in previous publications. For the case of laminar flows and  $Pr \gg 1$ , a particular flow development can be observed [13, 15], leading to several zones, as illustrated in Fig. 5:

- Region 1. The stagnation zone, of radial dimension  $r_1$  (studies found  $r_1$  to be ranging from  $d/2$  [12] to  $d$  [15]). It is characterized by an extremely thin thermal boundary layer  $\delta_t$ , resulting in large heat transfer.
- Region 2. Boundary layer ( $\delta < H_{film}$ ): a boundary layer type of flow develops along the wall. The velocity outside the viscous boundary layer  $\delta$  remains close to  $u_f$ . This region was analytically found to extend up to  $r_2 = 0.1773Re^{1/3}d$  [13, 15], where the viscous boundary layer  $\delta$  becomes as thick as the whole liquid film.
- Region 3. Viscous similarity region ( $\delta = H_{film}$  and  $\delta_t < H_{film}$ ): the film thickness is viscous over its entire height, affecting the growth of the thermal boundary layer  $\delta_t$ . For high  $Pr$ ,  $\delta_t$  will not reach the thickness of the liquid film before the hydraulic jump.
- Region 4. Hydraulic jump: the liquid film thickness increases abruptly, leading to a decrease in velocity and subsequently a deterioration of heat transfer. This complex phenomenon has been the object of dedicated studies [31, 32].

To illustrate this particular flow development for the present simulations, two cases are considered:  $Re = 290$  and  $Re = 1690$  (for  $Pr = 127$ ). These cases correspond to  $\dot{v} = 0.25$  and  $1.5 \text{ l.min}^{-1}$  for  $T_f = 343 \text{ K}$ ,  $T_s^{target} = 363 \text{ K}$ . Figure 6 shows for those two simulations the radial profiles of Nusselt number and the liquid/air interface along with the radial profiles of the viscous and thermal boundary layers,  $\delta$  and  $\delta_t$  respectively. For both cases, the first three regions are clearly noticeable. The stagnation zone, where heat transfer is maximum, extends up to  $r_1 \approx 0.6d$ . Both boundary layer profiles appear

quasi-constant in this region. The boundary layer regions extends up to  $r_2 = 0.1773Re^{1/3}d$  (in agreement with the literature), where the viscous boundary layer  $\delta$  reaches the film thickness. In region 3, the thermal boundary layer  $\delta_t$  keeps growing but, as predicted the layer never reaches the film thickness. The radial extension of the computational domain is too short to observe the hydraulic jump, even for the case with the lowest  $Re$  number.

Regarding heat transfer, it can be noticed in Fig. 6 that when  $Re$  increases,  $\delta$  (hence  $\delta_t$ ) decreases, leading to an increase in  $Nu$ . The radial decrease in heat transfer is directly related to the growth of thermal boundary layer. Concerning the heat transfer in the stagnation zone, the radial profiles of  $Nu$  are not constant in this area, unlike what is suggested by classical stagnation-point flow solution [28], and differ with the Reynolds number. This particular aspect is further investigated in Sec. 6.

### *5.2. Impact of the surface temperature on heat transfer*

Both experimental and simulation results show that an increase in surface temperature enhances heat transfer. To illustrate this effect, two cases with different surface temperatures are considered:  $T_s^{target} = 363$  and  $393 K$ , with  $T_f = 343 K$  and  $\dot{v} = 0.5 l.min^{-1}$ . The values of Reynolds and Prandtl numbers are ( $Re = 568$ ,  $Pr = 127$ ) and ( $Re = 788$ ,  $Pr = 93$ ), respectively. An increase in surface temperature leads to a higher film temperature. For the present cases, the average film temperature  $(T_f + T_s^{target})/2$  increases from  $353$  to  $368 K$ . This leads to a drop in dynamic viscosity by 35% (a strongly temperature-dependent property, as already noticed in [21]), as well as an increase in film velocity (confirmed by the lower film thickness for  $T_s^{target} = 393 K$  in Fig. 7a). These two effects increase the local Reynolds

number, leading to smaller boundary layer thicknesses  $\delta$  and subsequently  $\delta_t$  (as illustrated in Fig. 7a), despite the lower value of  $Pr$ . On average,  $\delta_t$  decreases by 15%, which is consistent with the increase in  $Nu$  depicted in Fig. 7b. The predominant effect of the local Reynolds number over the Prandtl number on the heat transfer illustrated in this example agrees with classic correlations of Nusselt number, as shown in next sections.

### 5.3. Non-assessed effects

Two additional effects reported in the literature were not assessed in the present cases: the nozzle-to-wall distance  $H$  and the nozzle diameter  $d$ . As summarized in [24], the nozzle-to-wall distance was found experimentally to have a limited and localized impact on heat transfer in the stagnation zone for  $1 < H/d < 20$  [22]. Within this range, increasing the nozzle-to-wall distance will tend to favor the diffusion of the jet velocity profile toward a uniform profile (as illustrated in Fig. 8), reducing heat transfer in the stagnation zone. For values of  $H/d$  lower than 1, simulations by [17] showed that the film gets thinner, with increasing heat transfer as  $H/d$  decreases, certainly due to a higher local Reynolds number. For the present cases, the ratio  $H/d$  remains equal to 5, which means that a variation in the nozzle-to-wall distance would not change drastically the conclusion presented here. Regarding the nozzle diameter  $d$ , a number of studies noted that higher Nusselt numbers are achieved when increasing  $d$  [19, 9, 24], more specifically in the stagnation zone. For ATF liquids, Renon et al. [24] found an almost linear dependency between  $d$  and the stagnation Nusselt number, meaning that the heat transfer coefficient is actually almost not impacted by a change in diameter, for fixed values of  $Re_j$  and  $Pr_j$ . It is assumed that the nozzle

diameter changes the flow dynamics, but dedicated studies should be carried out for further comprehension.

## 6. Characterization of heat transfer

### 6.1. Impact of the jet axial velocity on heat transfer in the stagnation zone

As mentioned in Sec. 5.1 and illustrated in Fig. 6, heat transfer in the stagnation zone is non-uniform and depends on the Reynolds number. For the case  $Re = 1690$  in Fig. 6b, it even displays a peak at  $r = 0.5d$ , and decreases slightly as the stagnation point is approached. This behavior has already been observed numerically [16, 17] and experimentally [4, 22]. It seems to be related to the axial velocity profile of the jet before impingement [17]. For the present simulations, the axial velocity profile at the nozzle inlet is uniform. As the flow progresses through the nozzle, a non-uniform velocity profile develops, although the nozzle is too short for this profile to be fully parabolic at the nozzle outlet, even for the cases with the lowest Reynolds number. When the distance to the wall decreases, the profile of the axial velocity of the jet tends to flatten under the effect of viscosity, as illustrated in Fig. 8, for cases  $Re = 290, 1690$  ( $Pr = 127$ ). For the jet with the smallest  $Re$ , the velocity profile at the nozzle exit is more developed than for the highest  $Re$ . Close to the wall, it is almost uniform, while for case  $Re = 1690$ , a dip in velocity profile occurs at  $r = 0.4d$ , causing the peak in  $Nu$  observed in Fig. 6b. Supplementary simulations were conducted to illustrate the effect of uniform and parabolic jet velocity profiles on the Nusselt number distribution. They are presented in Appendix B.

The characterization of the impact of the jet axial velocity on the heat

transfer in the stagnation zone has been the object of dedicated studies [33, 34, 14]. The flow within the stagnation zone can be divided into two zones: an outer region of inviscid flow and an inner viscous boundary layer region. Theory [34] shows that in the inviscid outer flow, the radial velocity evolves linearly with  $r$ :

$$\frac{u_r^{invisc.}}{u_f} = \frac{B r}{2 d} \quad (16)$$

where  $B$  is a constant, corresponding to an inviscid stagnation-point velocity gradient, which depends on the jet characteristics. The presence of the two zones, as well as the quasi-linear evolution of  $u_r^{invisc.}$  is verified in the present simulations, as illustrated in Fig. 9. It was shown in [34] that for high values of jet Weber number  $We_j$ ,  $B$  depends only on the jet axial velocity profile. For a perfectly uniform velocity profile,  $B$  tends analytically to 1.831, while for parabolic velocity profiles, the velocity gradient is nearly 2.5 times higher, with  $B = 4.646$  obtained analytically in [33] (value supported by experiments for  $0.05 < H/d \leq 6$ ), leading to increased heat transfer. In the present simulations, velocity profiles are neither fully uniform nor parabolic, so neither of these two values for  $B$  can apply directly. Instead, the constant  $B$  was computed for each simulation, considering the early stagnation zone, as shown in Fig. 9b for case  $Re = 290$ ,  $Pr = 127$ . The values of  $B$  range from 2.5 to 3.5, reflecting the various axial velocity profiles observed in the simulations.

## 6.2. Correlations for stagnation zone Nusselt number

At a constant nozzle-to-wall distance, correlations of Nusselt number at the stagnation zone  $Nu_0$  are expressed in the following form [33, 34, 28, 14,

22]:

$$Nu_0 = CRe^m Pr^n \quad (17)$$

where  $C$ ,  $m$  and  $n$  are analytically or empirically derived constants, which depend strongly on the type of liquid or the nozzle geometry. Usually,  $m$  is close to 0.5 for laminar flows and  $n \approx 1/3$  for high Prandtl numbers [22]. A similar formulation was analytically derived in [14], in which the square-root dimensionless velocity gradient  $\sqrt{B}$  accounts for the effect of arbitrary jet velocity profiles:

$$Nu_0 = CB^{1/2} Re^m Pr^n \quad (18)$$

In the present simulations, the laminar stagnation zone Nusselt number  $Nu_0$  is calculated as the spatial average of the Nusselt number over the stagnation zone:

$$Nu_0 = \frac{2}{r_1^2} \int_0^{r_1} r Nu(r) dr \quad (19)$$

with  $r_1 = 0.6d$ . Following the formulation in Eq. 18, and imposing  $n = 1/3$ , a correlation was obtained with a mean deviation of 4.45% (see Table 3) and plotted in Fig. 10:

$$Nu_0 = 0.586B^{1/2} Re^{0.53} Pr^{1/3} \quad (20)$$

A correlation similar to Eq. 17 can also be derived, but with a smaller coefficient of determination  $R^2$  and considerably larger mean and maximum deviation (see Table 3):

$$Nu_0 = 1.287Re^{0.49} Pr^{1/3} \quad (21)$$

This tends to confirm the relevancy of parameter  $B$  to account for the effect of the jet velocity distribution. In both cases, the value for the parameter  $m$  is very close to 0.5, which is close to experimental results [22, 24].

### 6.3. Radial distribution of heat transfer

Despite the limited radial extension of the computational domain ( $r/d \leq 3$ ), it remains interesting to study the radial distribution of the Nusselt number over the entire domain. Figure 11a presents five radial profiles of the Nusselt number, for cases covering the entire range of  $Re$  and  $Pr$  encountered in the dataset. As previously discussed in Sec. 5, the maximum heat transfer occurs in the stagnation region, then decreases with radial distance. Normalizing the Nusselt number profiles with the stagnation zone Nusselt number  $Nu_0$ , as presented in Fig. 11b, allows the data for  $r/d < 1$  to collapse relatively well. Beyond that, the normalized profiles decrease with  $Re$ . This slight dependency on  $Re$  has already been noticed in [22], where a correlation was developed to predict the Nusselt number profiles:

$$\frac{Nu}{Nu_0} = \frac{(\gamma Re)^{\zeta \frac{r}{d}}}{1 + \alpha \left(\frac{r}{d}\right)^\beta} \quad (22)$$

where  $\alpha, \beta, \gamma$  and  $\zeta$  are constants. For the present simulated database, those constants were determined by a least-squares approach, for  $r/d > 0.5$  (to discard the variability of the Nusselt profiles in the stagnation zone due to the difference in the axial velocity profiles of the jet):  $\alpha = 1.71$ ,  $\beta = 2.30$ ,  $\gamma = 0.99$ ,  $\zeta = 8.7 \times 10^{-2}$ . With these parameters, Eq. 22 correlates 95% of the dataset within 10%. The Nusselt number profiles scaled by  $Nu_0(\gamma Re)^{\zeta(r/d)}$ , presented in Fig. 11c, collapse very well into a single curve, which compares well to the correlation of Eq. 22. The coefficients differ slightly from those found in [22, 24] (particularly for  $\gamma$ ). This could be related to the limited radial extension of the domain in the present cases ( $r/d \leq 3$ ), compared to the other studies ( $r/d \leq 15$  and  $r/d \leq 10$  respectively). It is worth noting

that this correlation is only valid for  $r/d < 3$ , and should not be extrapolated to a wider domain.

The radial distributions of Nusselt correlations were compared to a recent correlation obtained by Renon et al. [24], for the case  $T_f = 343K$ ,  $T_s^{target} = 363K$  and  $\dot{v} = 1.5 l.min^{-1}$  ( $Re = 1694$ ,  $Pr = 127$ ). Figure 12 depicts the radial distributions of the Nusselt number obtained with the CHT simulation and the correlation of Eqs. 20 and 22: this correlation compares well to the simulation, with 3.5% of error on the average Nusselt number according to Table 4 (within the uncertainty of the experiment). The resulting radial profile of  $Nu$  derived from the Renon et al. [24] correlation, in dashed line in Fig. 12, is lower than that obtained for the CHT simulation (as well as the present correlation Eqs. 20 and 22) for the stagnation zone, but higher for  $r/d > 1$ , leading to an over-estimation of the average Nusselt number by almost 13% (see Table 4).

This result was expected, as the correlation in [24] was derived in conditions close to a uniform heat flux imposed at the wall, while the present cases are close to a uniform wall temperature. For uniform heat flux, the Nusselt number is higher than for uniform temperature (as shown analytically in [15]). This effect is reproduced numerically, by running a simulation with unchanged fluid conditions but imposing a uniform heat flux at the wall ( $\dot{q} = 128 kW/m^2$ ) instead of solving the CHT problem. The resulting Nusselt number distribution compares better to the correlation by Renon et al. in Fig. 12, particularly for  $r/d > 1.5$ . The Renon et al. correlation now slightly under-estimates the average Nusselt number of the simulation, by only 1.4%. The under-estimation of the Nusselt number up to  $r/d = 1.5$  by

the Renon et al. correlation is accentuated by the increase in  $Nu$  obtained by the simulation with uniform heat flux. If this barely impacts the average Nusselt number, it could locally lead to different temperature predictions. This difference could be attributed to different injection conditions, to the radially limited solid domain in the simulations or to the hypothesis of purely laminar flow considered for the present study. Further investigations would be required to fully validate the numerical predictions of heat transfer in the stagnation zone.

## 7. Grid sensitivity study

As already mentioned in Sec. 3.2, solving the thermal boundary layer for flows with high Prandtl numbers requires a fine grid along the wall, increasing dramatically the computational time. For the present simulation, the size of the computational domain is limited: the computational time associated to the resolution of the boundary layer remains manageable. However, simulating direct oil cooling of a representative electric machine would entail larger geometries, for which such a fine grid cannot be considered. In this context, it is interesting to investigate the sensitivity of heat transfer predictions to the grid resolution in the liquid film, with the objective to propose an optimal grid strategy (minimizing computational cost while ensuring accuracy of heat transfer). A grid sensitivity study was conducted for the case  $\dot{v} = 1.5 \text{ l.min}^{-1}$ ,  $T_f = 343 \text{ K}$ , with two targeted surface temperatures  $T_s^{target} = 363$  and  $393 \text{ K}$ , to investigate the effect of a variation of heat flux. In addition to the reference grid (with  $\Delta_{z,min} = 3 \mu\text{m}$ ), 7 other grids were tested, by varying the first cell size  $\Delta_{z,min}$  and keeping a fixed expansion

ratio. The number of cells within  $\delta_t$  progressively decreases, as depicted in Fig. 13a for the case  $T_s^{target} = 363 K$ :

- for  $\Delta_{z,min} = 3, 5$  and  $10 \mu m$ : between 1 to 5 cells within  $\delta_t$  in the stagnation zone (and up to 12 cells when increasing  $r$  for the finest resolution);
- for  $\Delta_{z,min} = 20, 30, 40, 60$  and  $100 \mu m$ : no cell within  $\delta_t$  in the stagnation zone, and a decreasing resolution of  $\delta_t$  in the rest of the film. For  $\Delta_{z,min} = 60$  and  $100 \mu m$ , there is no cell within the entire radial extend of  $\delta_t$ .

To differentiate the resolution of thermal and hydrodynamic boundary layers, the total number of cells within  $\delta$  (or the film thickness  $H_{film}$  for  $r/d > 2.1$ ) is shown in Fig. 13b for the coarser grids (starting from  $\Delta_{z,min} = 20 \mu m$ ). For the case  $\Delta_{z,min} = 20 \mu m$ , a minimum resolution of 4 cells within  $\delta$  in the stagnation zone, and up to 8 cells within the film thickness as  $r$  increases, ensure a reasonable resolution of the viscous flow. It rapidly degrades for higher values of  $\Delta_{z,min}$ . For  $\Delta_{z,min} = 100 \mu m$ , there is only one cell within  $\delta$  for  $r/d > 1$ , which suggests an insufficient resolution of the hydrodynamic flow field. When increasing the surface temperature,  $\delta$  and  $\delta_t$  gets thinner, as discussed in Sec. 5. However, for an increase in  $T_s^{target}$  from 363 to 393 K, it was shown in Fig. 7a that the reduction in boundary layer thicknesses is very limited (less than 10%), thus the resolution of the boundary layers for the case  $T_s^{target} = 393 K$  can be considered similar as for the case  $T_s^{target} = 363 K$ , presented in Fig. 13. The impact of the grid refinement on the Nusselt number distribution is depicted in Fig. 14 for the case  $T_s^{target} = 363 K$ . For

$\Delta_{z,min} = 5$  and  $10 \mu m$ , a slight shift of the profile can be observed compared to the reference case  $\Delta_{z,min} = 3 \mu m$ , up to  $r/d = 0.75$  and  $1.25$  respectively. From  $\Delta_{z,min} = 20 \mu m$ , the Nusselt number distribution is no longer captured in the vicinity of the stagnation zone. As  $\Delta_{z,min}$  increases, the profiles are shifted further away, underestimating the heat transfer more and more. The relative change in surface-averaged Nusselt number and surface temperature compared to the reference grid are shown in Fig. 15a and Fig. 15b, respectively, for both targeted surface temperatures. As noticed on the radial distributions of  $Nu$ , the error in  $\overline{Nu}$  and thus  $\overline{T_s}$  increases as the grid resolution decreases, but remains very low up to  $\Delta_{z,min} = 20 \mu m$ , showing the negligible impact of a low resolution of  $\delta_t$  in the stagnation zone on the overall heat transfer. This is expected, as cooling in the stagnation zone represents a limited fraction of the heat transfer on the entire target surface. This fraction can be evaluated as follows:

$$\epsilon = \frac{\int_0^{0.6d} r Nu dr}{\int_0^R r Nu dr} \quad (23)$$

where the numerator and the denominator are the Nusselt number distributions averaged over the stagnation zone (which was found to range from  $r = 0$  to  $r = 0.6d$  in Sec. 5) and the entire surface of radius  $R$ , respectively. The fraction  $\epsilon$  therefore represents the proportion of total heat transfer directly related to the stagnation zone. Among all cases,  $\epsilon$  was found to be less than 10%, meaning the heat transfer in the stagnation zone represents less than 10% of the overall cooling of the surface. This percentage will obviously decrease if a wider surface is considered: the larger the target to be cooled, the smaller the impact of the stagnation zone on the overall heat transfer. If a fine resolution of  $\delta_t$  in the stagnation zone does not seem necessary for

accurate heat transfer prediction, however, the errors increase dramatically when there is no cell within  $\delta_t$  in the entire radial range ( $\Delta_{z,min} = 60$  and  $100 \mu m$ ): up to 25% error on  $\overline{T_s}$  and 60% on  $\overline{Nu}$ . A grid with no cell within  $\delta_t$  entails a minimum error in heat transfer prediction of 40%, but the error for the surface temperature remains relatively small (no more than 25% for the present simulations), as  $\left| \frac{dh}{h} \right| = \left| \frac{dT_s}{T_s - T_f} \right|$ . Finally, Fig. 15b shows that the error in surface temperature prediction increases with the heat flux value (or  $T_s^{target}$  in the present case), unlike the error on  $\overline{Nu}$  which remains constant. For  $\Delta_{z,min}$  less or equal to  $20 \mu m$  though, the error on the surface temperature remains negligible. In conclusion, the limited contribution of the stagnation zone to the overall heat transfer on the target surface means that the thermal boundary layer can be under-resolved in this region (with a minimum of one cell within  $\delta_t$ ) without impacting considerably the local and surface-averaged heat transfer prediction. However, a few cells (minimum 2 to 3) within  $\delta_t$  are required in the rest of the computational domain for an accurate prediction of heat transfer.

## 8. Conclusions

This study presented 3D simulations of laminar oil jets impinging on a flat, heated target, using the VoF method to model the two-phase flow and a CHT approach to calculate heat transfer. Particular attention was given to the grid definition in the film, to ensure a proper resolution of heat transfer without using any wall law. Over 20 simulations were performed, including parameter variations as conducted in the experiments [21] (fluid temperature, flow rate, heat flux). Practically all simulated cases yield a surface-averaged

Nusselt number within the uncertainty range of the experimental results. The structure of the flow was analyzed (via a characterization of hydrodynamics and thermal boundary layers) and agrees with current knowledge from the literature. As observed in the experiments, an increase in surface temperature translates into an increase in the Nusselt number: the higher film temperature leads to a decrease in the dynamic viscosity of the oil film resulting in an increase in film velocity. Then, heat transfer results were characterized. The correlation between the jet axial velocity profiles and the heat transfer in the stagnation zone was observed and quantified by the radial dimensionless velocity gradient  $B$ , as depicted in the literature. Nusselt number correlations for the stagnation zone were derived, showing a similar dependency in terms of  $Re$  or  $Pr$  as in previous experimental studies for high  $Pr$  impinging jets. A correlation for the radial distribution of Nusselt number was also derived, following an equation used in previous studies of high  $Pr$  impinging jets. Comparison to previous experiments is however complicated by the differences in the setups (uniform wall temperature versus uniform heat flux, injector geometries). Finally, a grid sensitivity study showed that the thermal boundary layer can be under-resolved in the stagnation zone (with a minimum of one cell within  $\delta_t$ ), introducing only a minor error in local and surface-averaged heat transfer prediction. However, not solving at all the thermal boundary layer could entail a minimum error of 40% in average heat transfer prediction. A minimum number of cells (2 to 3) within the thermal boundary layer was found to be necessary for accurate predictions of heat transfer. This requirement can induce a too high computational time for full-scaled simulations of oil cooling of electric machines.

Future work will then focus on the development of a specific sub-grid model, allowing predictive simulations on realistic geometries with a computational time compatible with industrial requirements. The fully resolved simulations in the present article can be used as a reference to elaborate and validate such a model.

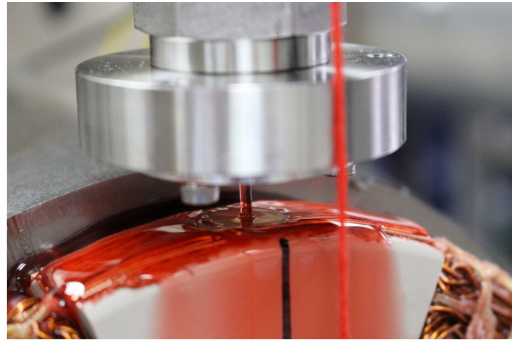
### **Declaration of Competing Interest**

The authors declare that they have no known competing financial interests or personal relationships that could have appeared to influence the work reported in this paper.

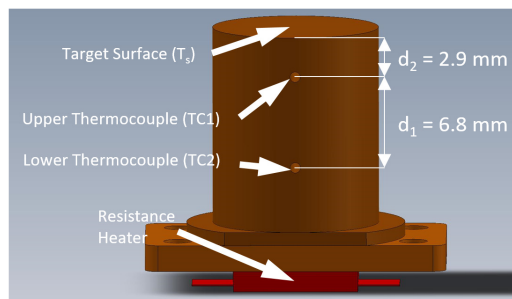
### **Acknowledgements**

The numerical part of the work was carried out and funded at IFPEN as part of an internal research project. All calculations were performed on the IFPEN supercomputer. This work was authored in part by the Alliance for Sustainable Energy, LLC, the manager and operator of the National Renewable Energy Laboratory for the U.S. Department of Energy (DOE) under Contract No. DE-AC36-08GO28308. Funding was provided by the U.S. Department of Energy Office of Energy Efficiency and Renewable Energy Vehicle Technologies Office Electric Drive Technologies Program. The views expressed in the article do not necessarily represent the views of the DOE or the U.S. Government. The U.S. Government retains and the publisher, by accepting the article for publication, acknowledges that the U.S. Government retains a nonexclusive, paid-up, irrevocable, worldwide license to publish or

reproduce the published form of this work, or allow others to do so, for U.S. Government purposes.



(a)



(b)

Figure 1: (a) Photo of the experimental setup depicting the liquid jet impinging the target embedded in the housing and (b) schematic of the heated target assembly.

Table 1: Variation of experimental parameters used in the simulations.

Parameter	Values
Fluid temperature, $T_f$ (K)	323, 343, 363
Fluid flow rate, $\dot{v}$ ( $l.min^{-1}$ )	0.25, 0.5, 1.0, 1.5
Target surface temperature, $T_s^{target}$ (K)	363*, 373**, 393***

\*Only for  $T_f = 323$  and  $343K$ ; \*\*Only for  $T_f = 363K$ ; \*\*\*For all 3 values of  $T_f$

Table 2: Liquid and solid properties as a function of temperature (K).

Properties curve fit	$R^2$	Unit	Source
Liquid properties			
$c_p(T) = 3.829T + 907.13$	0.998	$J/(kg \cdot K)$	Ford
$\rho(T) = -0.64T + 1027.6$	1	$kg/m^3$	Ford
$\ln(\mu(T)) = 1.05 \times 10^{-4}T^2 - 0.0992T + 16.991$	0.995	$kg/(m \cdot s)$	Ford
$k = 0.13$	-	$W/(m \cdot K)$	Ford
$\sigma(T) = -8.0 \times 10^{-5}T + 0.0582$	1	$N/m$	[27]
Solid properties			
$c_p = 386.0$	-	$J/(kg \cdot K)$	[35]
$\rho = 8.93 \times 10^3$	-	$kg/m^3$	[35]
$k(T) = -0.0749T + 423.2$	0.9986	$W/m \cdot K$	[36]

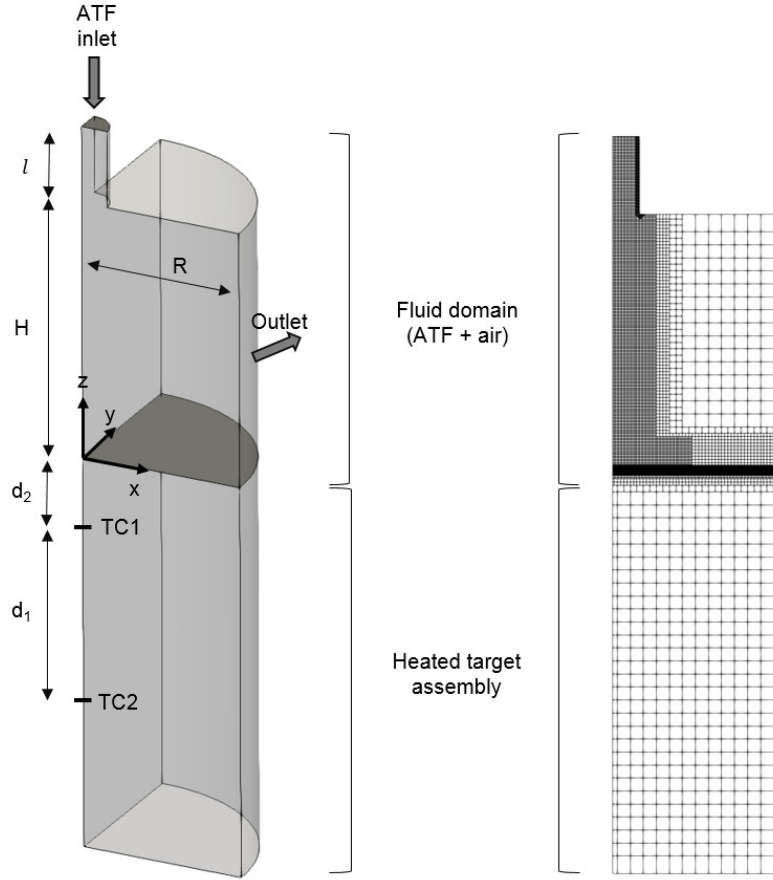
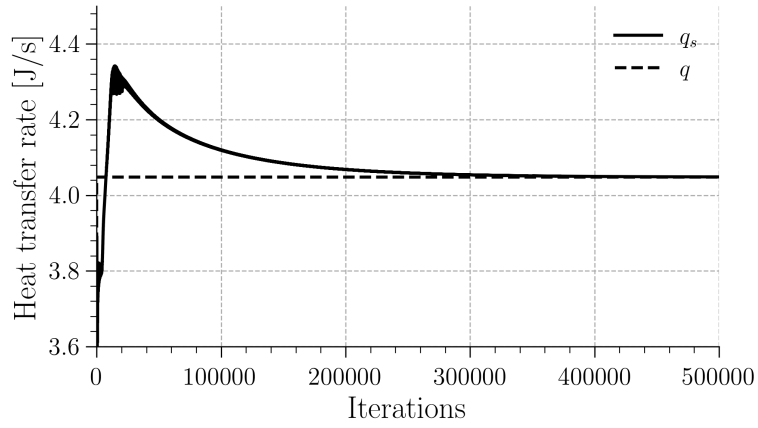


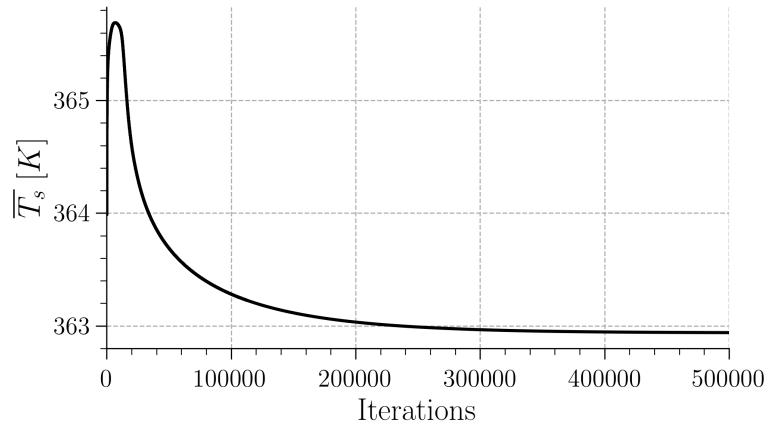
Figure 2: Computational domain (left) showing the fluid and solid regions, and computational grid (right), with refinement in the nozzle, in the liquid region and along the impinging wall.

Table 3: Stagnation zone Nusselt number correlations obtained from simulations.

Correlation		$R^2$	Mean (max.) deviation (%)
$Nu_0 = 0.586B^{1/2}Re^{0.53}Pr^{1/3}$	Eq. 20	0.9805	4.45 (10.7)
$Nu_0 = 1.287Re^{0.49}Pr^{1/3}$	Eq. 21	0.9581	7.0 (19.8)

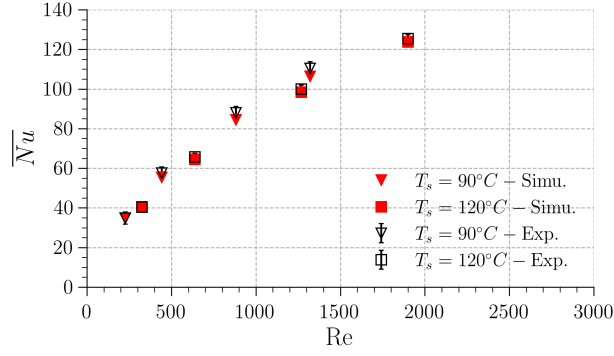


(a)

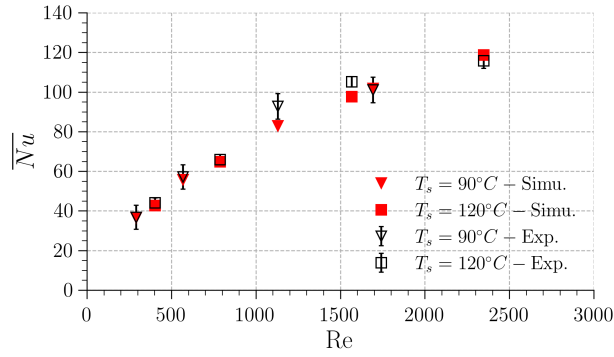


(b)

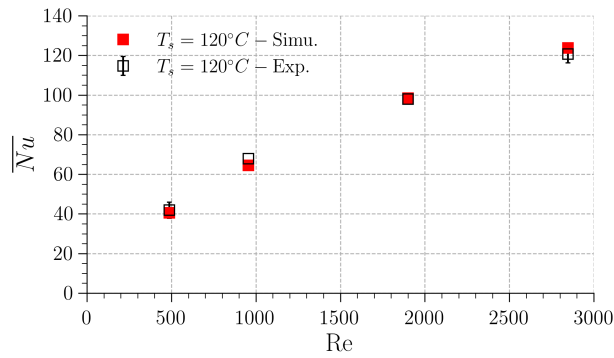
Figure 3: Evolution of (a) the heat transfer rate at the target surface  $q_s$  compared to the value imposed at the bottom target  $q$ , and (b) the average surface temperature  $T_s$  during the simulation.



(a)  $T_f = 323K$



(b)  $T_f = 343K$



(c)  $T_f = 363K$

Figure 4: Comparison of the average Nusselt number from experimental and numerical results for (a)  $T_f = 323K$ , (b)  $T_f = 343K$  and (c)  $T_f = 363K$ . Error bars on measurements are represented when available.

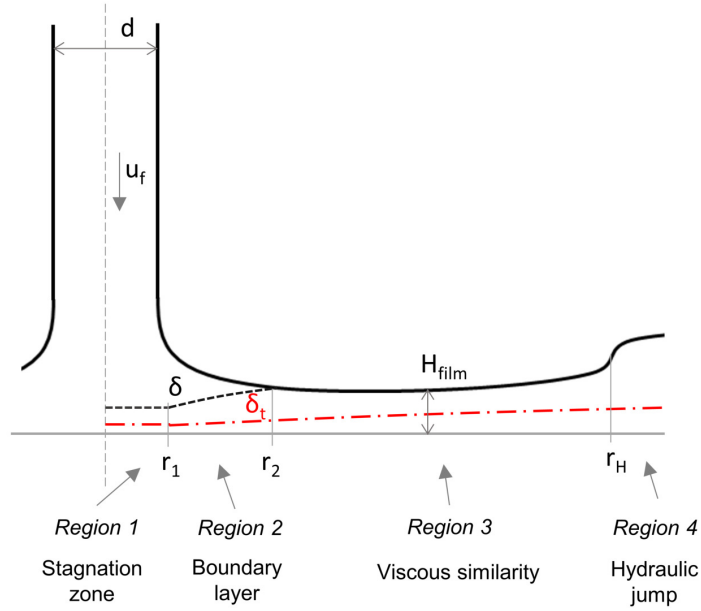


Figure 5: Downstream development of a laminar, axisymmetric impinging jet for  $Pr \gg 1$ .

Table 4: Surface-averaged Nusselt number  $\overline{Nu}$  for the case  $T_f = 343K$ ,  $T_s^{target} = 363K$  and  $\dot{v} = 1.5 l.min^{-1}$  ( $Re = 1694$ ,  $Pr = 127$ ).

Experiment	Simulations		Correlations	
	CHT	unif. $\dot{q}$	Eqs. 20 and 22	Renon et al. [24]
101.0	101.8	117.2	98.3	115.5

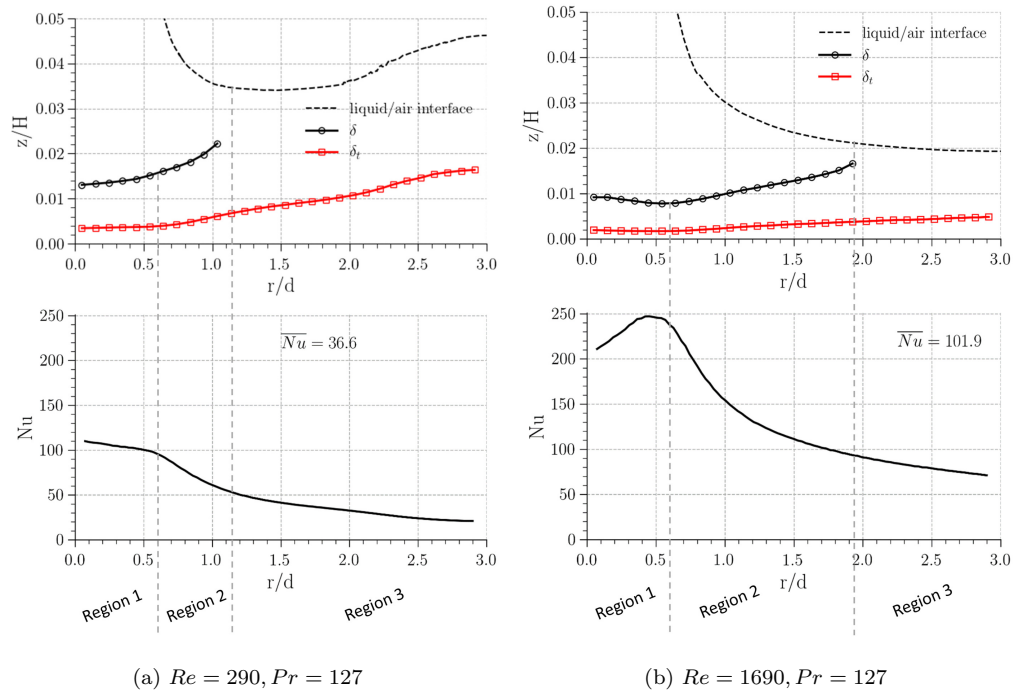
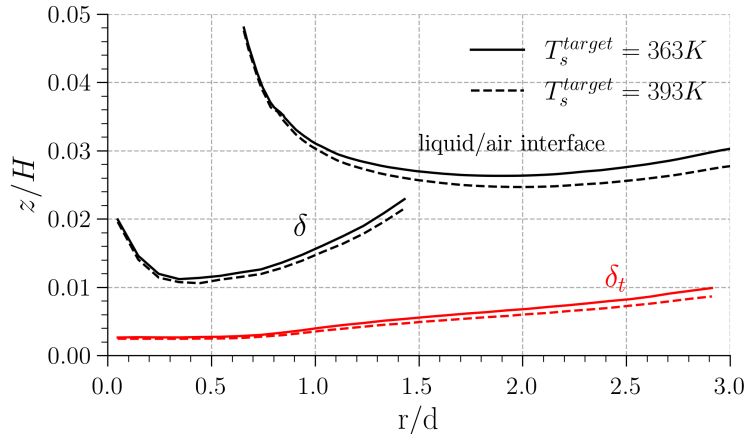
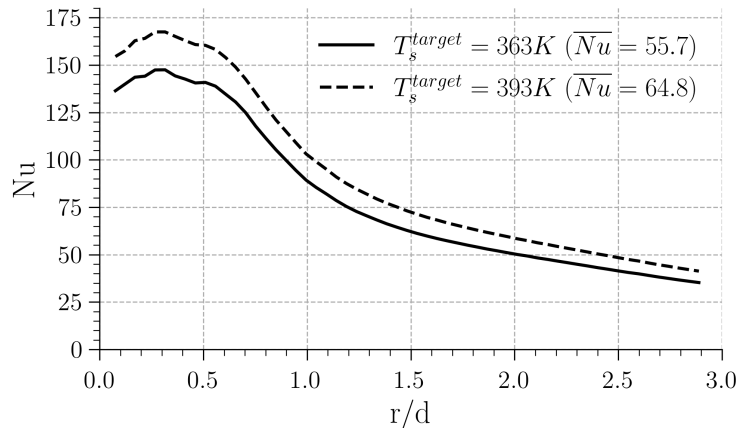


Figure 6: Radial profiles of liquid/air interface,  $\delta$  and  $\delta_t$  (top) and radial profiles of Nusselt number  $Nu$  (bottom) for (a)  $Re = 290, Pr = 127$  and (b)  $Re = 1690, Pr = 127$ .



(a)



(b)

Figure 7: Radial profiles of (a) liquid/air interface,  $\delta$  and  $\delta_t$  and (b) Nusselt number for  $T_s^{target} = 363$  and  $393K$  ( $T_f = 343K$  and  $\dot{v} = 0.5l.min^{-1}$ ).

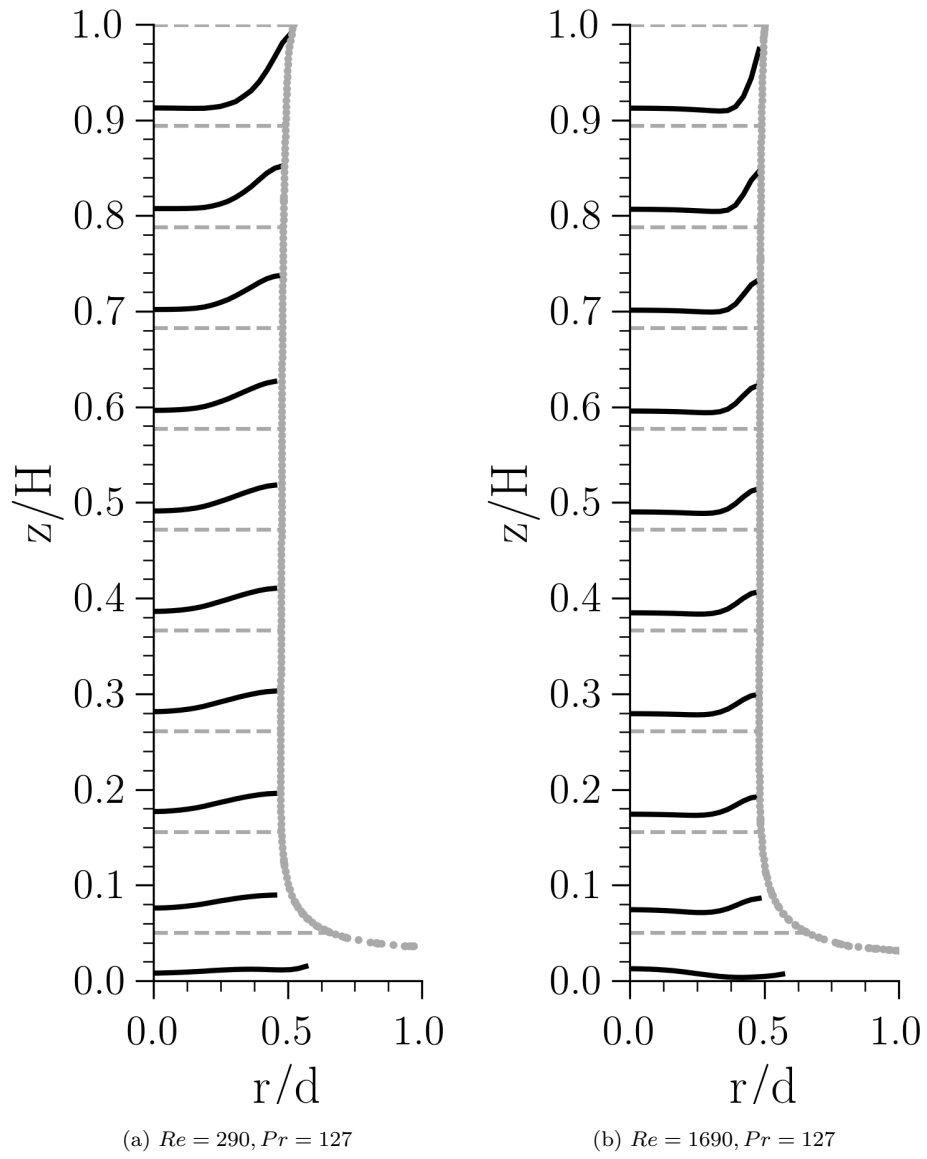
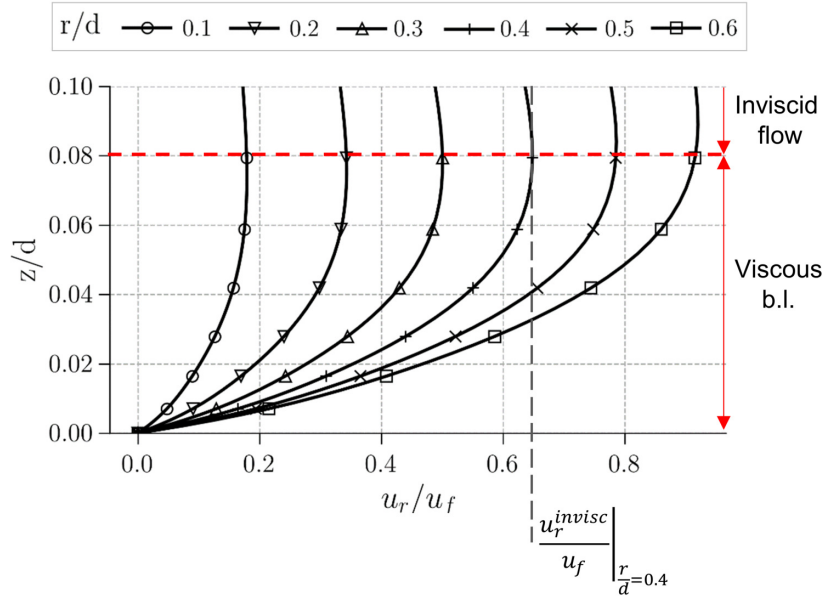
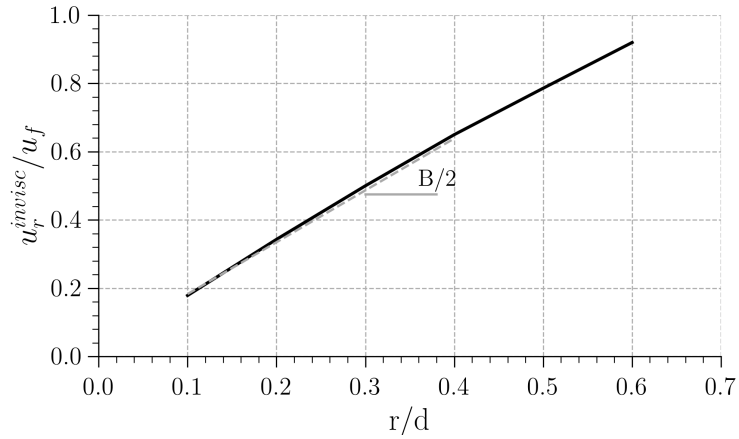


Figure 8: Radial profiles of axial velocity in the jet, at various axial location (grey lines), for (a)  $Re = 290, Pr = 127$  and (b)  $Re = 1690, Pr = 127$ .



(a)



(b)

Figure 9: (a) Profiles of radial velocity  $u_r$  at various radial location within the stagnation zone (for illustration purposes, the value for velocity  $u_r^{invisc}$  at  $r/d = 0.4$  is noted) and (b) radial evolution of  $u_r^{invisc}$  with linear curve fit with  $B = 2.95$ , for  $Re = 290$ ,  $Pr = 127$ .

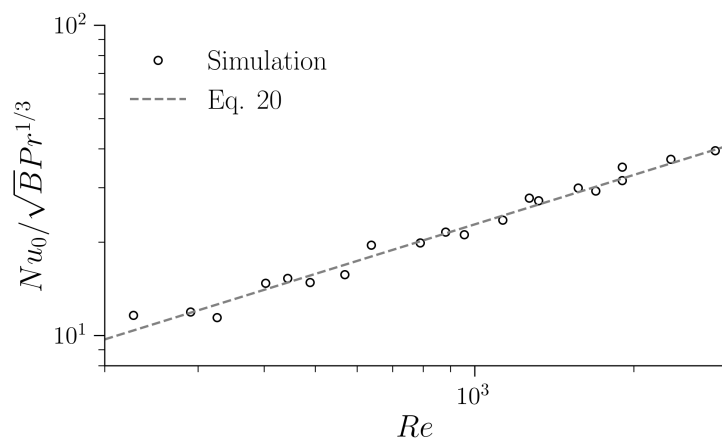
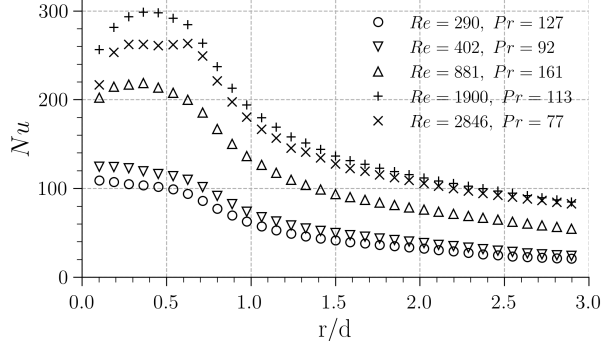
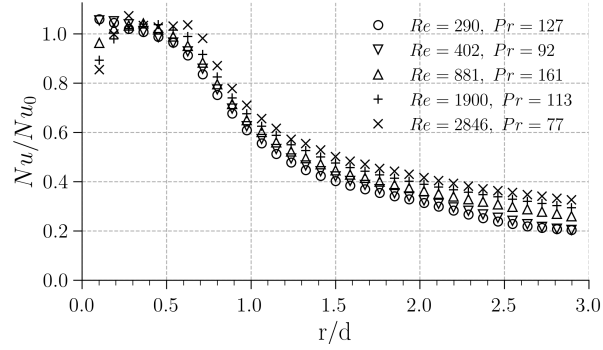


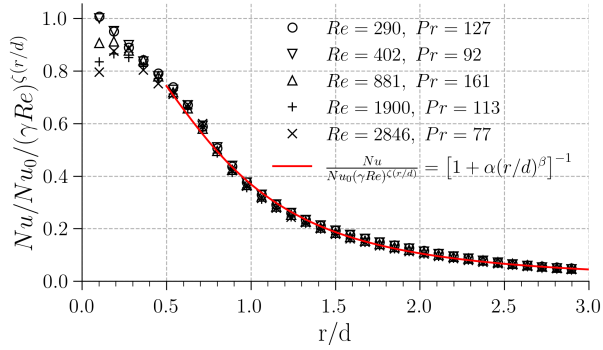
Figure 10: Correlation of the stagnation zone Nusselt number  $Nu_0$  based on simulation data, using dimensionless parameters  $B$ ,  $Re$  and  $Pr$ .



(a)



(b)



(c)

Figure 11: Radial distribution of Nusselt number (a), non-dimensionalized by (b)  $Nu_0$  and by (c)  $Nu_0(\gamma Re)^{\zeta(r/d)}$  with  $\gamma = 0.99$ ,  $\zeta = 8.7 \times 10^{-2}$ , for various volumetric flow rates, jet and surface temperatures. In Fig. (c), the curve fit uses the following constants  $\alpha = 1.71$ ,  $\beta = 2.30$ .

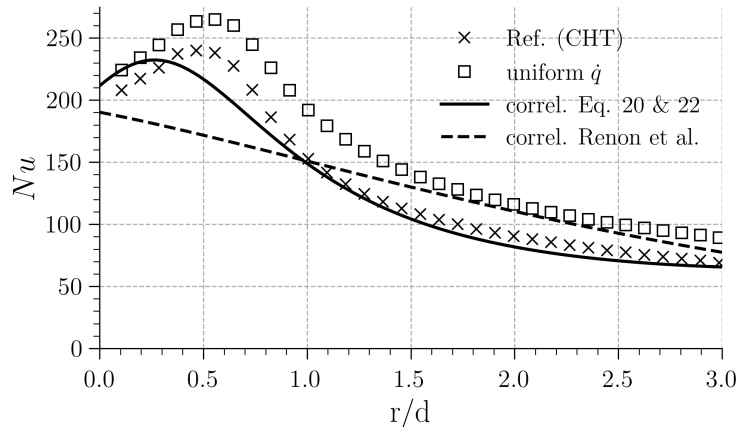
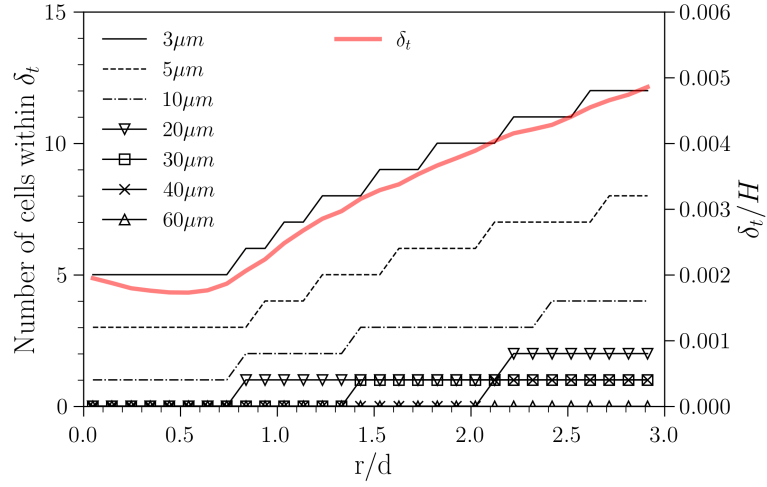
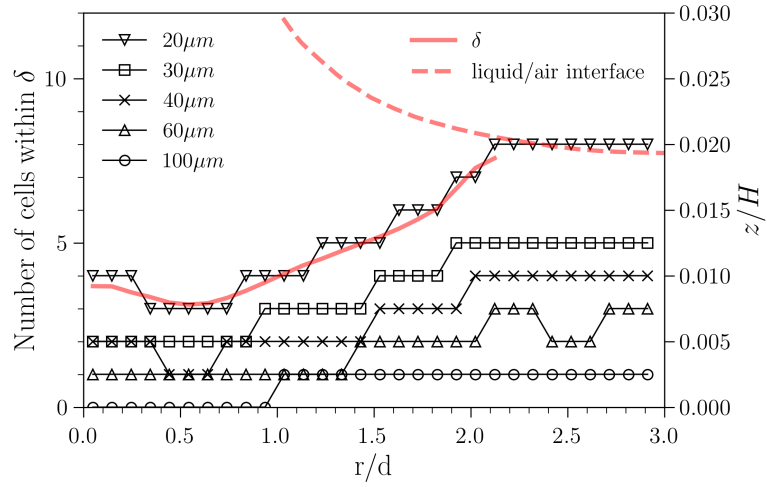


Figure 12: Radial distributions of Nusselt number for the case  $T_f = 343K$ ,  $T_s^{target} = 363K$  and  $\dot{v} = 1.5 l.min^{-1}$  ( $Re = 1694$ ,  $Pr = 127$ ) obtained from numerical simulations (reference CHT setup and imposing a uniform heat flux), and from correlations (Eqs. 22 and 20) of the present study and correlation from Renon et al. [24].



(a) Number of cells within  $\delta_t$ .



(b) Number of cells within  $\delta$  ( $r/d < 2.1$ ) or within  $H_{film}$  ( $r/d > 2.1$ ).

Figure 13: Number of cells within (a)  $\delta_t$  and (b)  $\delta$  (or  $H_{film}$ ) for various grid resolutions  $\Delta_{z,min}$ , for case  $\dot{v} = 1.5 l.min^{-1}$ ,  $T_f = 343 K$  and  $T_s^{target} = 363 K$ .

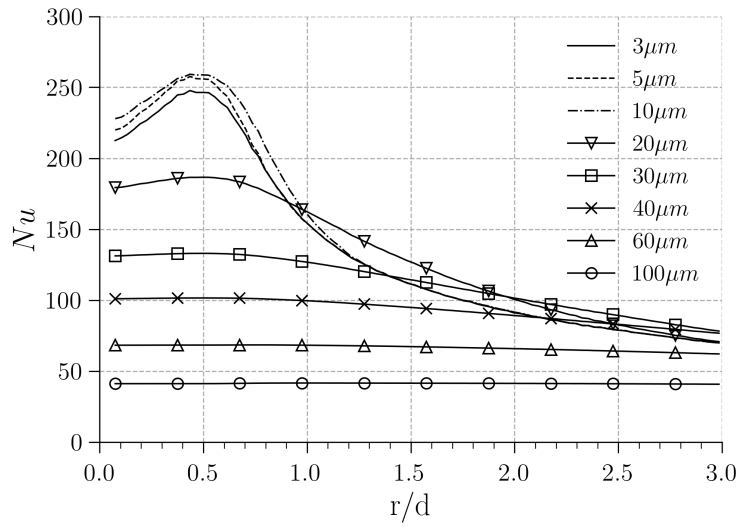
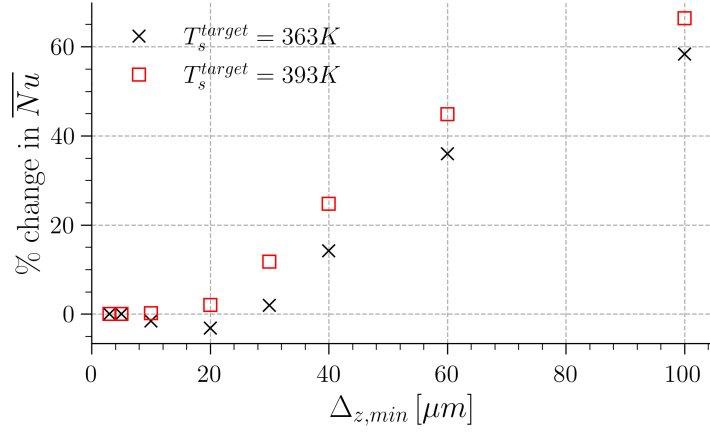
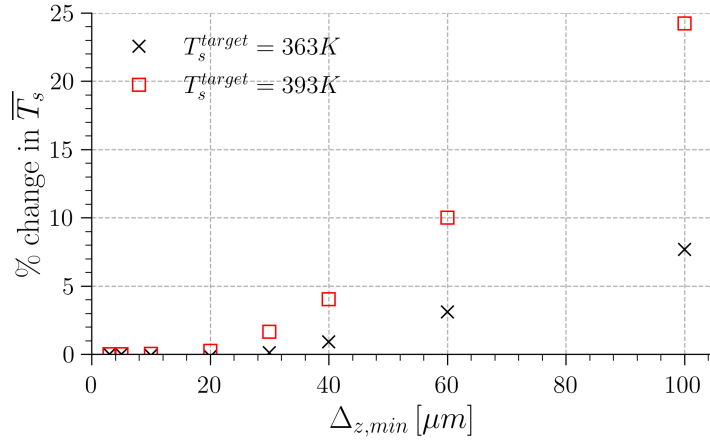


Figure 14: Radial distributions of Nusselt number for various grid resolutions  $\Delta_{z,min}$ , for case  $\dot{v} = 1.5 \text{ l.min}^{-1}$ ,  $T_f = 343 \text{ K}$  and  $T_s^{target} = 363 \text{ K}$ .



(a)



(b)

Figure 15: Relative change in surface-averaged Nusselt number (a) and temperature (b) compared to the reference grid ( $\Delta_{z,min} = 3\mu m$ ) for case  $\dot{v} = 1.5 l.min^{-1}$ ,  $T_f = 343 K$  and two targeted surface temperatures.

## Appendix A. Viscous dissipation effect

In the literature, to account for heating due to viscous dissipation, the adiabatic wall temperature  $T_{aw}$  is usually considered in the definition of heat transfer coefficient:

$$h = \frac{\dot{q}}{T_s - T_{aw}} \quad (\text{A.1})$$

The adiabatic wall temperature can be obtained from the following equation

$$T_{aw} = T_f + r \frac{u_f^2}{2c_p} \quad (\text{A.2})$$

where  $r$  is a recovery factor, whose distribution varies radially. Experimental measurements performed for impinging liquid jet with high  $Pr$  number [37, 22] found that  $r$  mainly depends on  $Pr$ . The following correlation was found in [22] for the maximum value of  $r$ :

$$r_{max} = 5.53Pr^{0.24} \quad (\text{A.3})$$

Based on Eqs. A.2-A.3, a maximum value for the temperature difference  $T_{aw} - T_f$  can be estimated. Among all the simulated cases, this difference would be maximum for the case with minimal liquid and surface temperature (so  $T_f = 323 \text{ K}$  and  $T_s^{target} = 363 \text{ K}$ ), giving the highest values for both  $Pr$  and  $c_p$  (resp. 161 and 2208  $J/(kgK)$ ), and for the highest flow rate  $\dot{v} = 1.5 \text{ l.min}^{-1}$  (giving  $u_f = 7.5 \text{ m.s}^{-1}$ ). This gives a maximum value  $T_{aw} - T_f = 0.24 \text{ K}$ . To confirm this estimation, a simulation was performed in those conditions, imposing a zero heat flux at the wall. The resulting surface temperature then corresponds to  $T_{aw}$ . The simulation gives similar predictions compared to the estimation, with  $T_{aw} - T_f = 0.21 \text{ K}$ . This value is small enough to be neglected: estimating the heat transfer coefficient  $h$  using Eq. 13 is relevant.

If higher velocities (larger than  $15 \text{ m.s}^{-1}$ ) were considered,  $T_{aw} - T_f$  would become larger than  $1K$ , which would not be negligible anymore.

## Appendix B. Impact of the jet axial velocity profile on the distribution of Nusselt number

As discussed in Sec. 5, for the simulated cases, the radial distribution of  $Nu$  in the stagnation zone seems to be related to the axial velocity profile at the nozzle exit. To illustrate the variability in local Nusselt number, two additional simulations were performed for the case  $T_f = 343 K$ ,  $T_s^{target} = 363 K$  and  $\dot{v} = 1.5 \text{ l.min}^{-1}$  ( $Re = 1690$ ,  $Pr = 127$ ). The nozzle was removed from the computational domain, imposing instead of the nozzle outlet an inlet boundary condition, with a fixed velocity profile. For one case, a uniform velocity profile  $u_z = -u_f = -7.5 \text{ m.s}^{-1}$  is imposed. For the second case, a parabolic velocity profile is fixed:

$$u_z(r) = -u_{z,max} \left[ 1 - \left( \frac{2r}{d} \right)^2 \right] \quad (\text{B.1})$$

with  $u_{z,max} = 2u_f$ . The resulting radial distribution of the Nusselt number is depicted in Fig. B.16, along with the reference case for which the flow in the nozzle is simulated. As noticed in Sec. 5, heat transfer is impacted by the jet velocity profile mostly in the stagnation zone region. For the case with the parabolic velocity profile, the maximum amplitude of the Nusselt number is more than twice that of the uniform velocity profile, and is reached at the stagnation point for the case with the parabolic velocity profile. Over the entire surface of the target, the average Nusselt number is increased by 9% when a parabolic velocity profile is applied compared to a uniform velocity

profile. Accounting for the nozzle geometry in CFD simulation is therefore crucial for an accurate prediction of heat transfer, both locally and globally. For reference, the values for the constant  $B$ , accounting for the impact of the axial velocity profile of the jet for the Nusselt correlation in the stagnation zone (Eq. 20) are 1.95 and 4.4 for the uniform and parabolic velocity profile, respectively. They are in good agreement with the theory, which predicts 1.831 and 4.646 respectively. A similar influence of the axial velocity profile was observed in other numerical studies [17], and experimentally in [22], where two nozzles were tested for high  $Pr$  number impinging jets: a pipe-type nozzle (which would give parabolic velocity profiles at the nozzle exit) and an orifice-type nozzle (closer to uniform velocity profiles). The radial distribution of Nusselt number clearly showed a plateau-like shape in the stagnation zone for the orifice nozzle, while a peak in  $Nu$  can be noticed for the pipe nozzle, with higher values for similar Reynolds number. The Nusselt correlations derived from measurements also reflected this effect.

## References

- [1] T. Davin, J. Pellé, S. Harmand, R. Yu, Experimental study of oil cooling systems for electric motors, *Applied Thermal Engineering* 75 (2015) 1–13. doi:<https://doi.org/10.1016/j.applthermaleng.2014.10.060>.
- [2] C. Liu, Z. Xu, D. Gerada, J. Li, C. Gerada, Y. C. Chong, M. Popescu, J. Goss, D. Staton, H. Zhang, Experimental investigation on oil spray cooling with hairpin windings, *IEEE Transactions on Industrial Electronics* 67 (9) (2020) 7343–7353. doi:[10.1109/TIE.2019.2942563](https://doi.org/10.1109/TIE.2019.2942563).

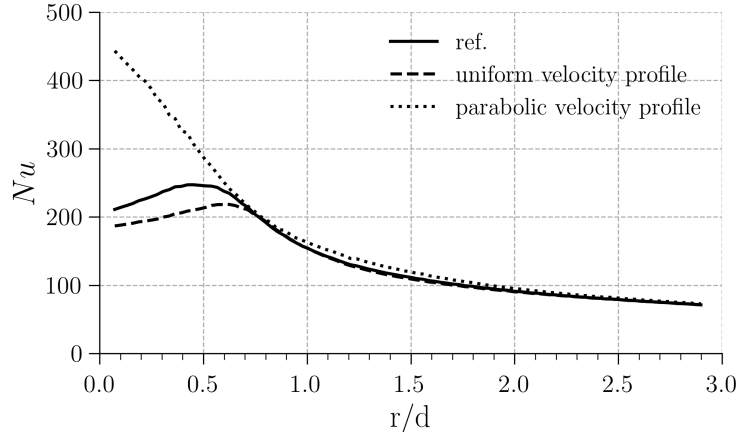


Figure B.16: Radial distributions of Nusselt number for the case  $T_f = 343\text{ K}$ ,  $T_s^{target} = 363\text{ K}$  and  $\dot{v} = 1.5\text{ l.min}^{-1}$ , solving the flow in the nozzle (ref.) or imposing a uniform or parabolic velocity profile at the nozzle exit.

- [3] R. Sindjui, G. Zito, S. Zhang, Experimental study of systems and oils for direct cooling of electrical machine, *Journal of Thermal Science and Engineering Applications* 14 (5) (2021). doi:10.1115/1.4051934.
- [4] Y. Pan, J. Stevens, B. W. Webb, Effect of Nozzle Configuration on Transport in the Stagnation Zone of Axisymmetric, Impinging Free-Surface Liquid Jets: Part 2—Local Heat Transfer, *Journal of Heat Transfer* 114 (4) (1992) 880–886. doi:10.1115/1.2911896.
- [5] D. T. Vader, F. P. Incropera, R. Viskanta, Local convective heat transfer from a heated surface to an impinging, planar jet of water, *International Journal of Heat and Mass Transfer* 34 (3) (1991) 611–623. doi:10.1016/0017-9310(91)90110-Z.
- [6] J. Stevens, B. W. Webb, Local Heat Transfer Coefficients Under an

- Axisymmetric, Single-Phase Liquid Jet, *Journal of Heat Transfer* 113 (1) (1991) 71–78. doi:10.1115/1.2910554.
- [7] J. Stevens, B. W. Webb, Measurements of flow structure in the radial layer of impinging free-surface liquid jets, *International Journal of Heat and Mass Transfer* 36 (15) (1993) 3751–3758.
- [8] C.-Y. Li, S. V. Garimella, Prandtl-number effects and generalized correlations for confined and submerged jet impingement, *International Journal of Heat and Mass Transfer* 44 (18) (2001) 3471–3480. doi:10.1016/S0017-9310(01)00003-5.
- [9] J. B. Baonga, H. Louahlia-Gualous, M. Imbert, Experimental study of the hydrodynamic and heat transfer of free liquid jet impinging a flat circular heated disk, *Applied Thermal Engineering* 26 (11-12) (2006) 1125–1138. doi:10.1016/j.applthermaleng.2005.11.001.
- [10] E. J. Watson, The radial spread of a liquid jet over a horizontal plane, *Journal of Fluid Mechanics* 20 (3) (1964) 481–499. doi:10.1017/S0022112064001367.
- [11] Wang, X. S., Dagan, Z., Jiji, L. M., Conjugate heat transfer between a laminar impinging liquid jet and a solid disk, *Int. J. Heat Mass Transfer* 32 (11) (1989).
- [12] X. S. Wang, Z. Dagan, L. M. Jiji, Heat transfer between a circular free impinging jet and a solid surface with non-uniform wall temperature or wall heat flux—1. Solution for the stagnation region, *Inter-*

- national Journal of Heat and Mass Transfer 32 (7) (1989) 1351–1360. doi:10.1016/0017-9310(89)90034-3.
- [13] X. Liu, J. Lienhard, Liquid jet impingement heat transfer on a uniform flux surface, *Heat Transfer Phenomena in Radiation, Combustion, and Fires* 106 (1989) 523–530.
- [14] J. H. Lienhard, Liquid jet impingement, *Annual Review of Heat Transfer* 6 (6) (1995) 199–270. doi:10.1615/AnnualRevHeatTransfer.v6.60.
- [15] C. F. Ma, Y. H. Zhao, T. Masuoka, T. Gomi, Analytical study on impingement heat transfer with single-phase free-surface circular liquid jets, *Journal of Thermal Science* 5 (4) (1996) 271–277. doi:10.1007/BF02653234.
- [16] H. Fujimoto, N. Hatta, R. Viskanta, Numerical simulation of convective heat transfer to a radial free surface jet impinging on a hot solid, *Heat and Mass Transfer* 35 (4) (1999) 266–272. doi:10.1007/s002310050323.
- [17] A. Y. Tong, A numerical study on the hydrodynamics and heat transfer of a circular liquid jet impinging onto a substrate, *Numerical Heat Transfer, Part A: Applications* 44 (1) (2003) 1–19. doi:10.1080/713838171.
- [18] B. Edin, Š. Šefko, Computational Modeling and Simulation of Nonisothermal Free-surface Flow of a Liquid Jet Impinging on a Heated Surface, *Procedia Engineering* 100 (2015) 115–124. doi:10.1016/j.proeng.2015.01.349.
- [19] J. E. Leland, M. R. Pais, Free Jet Impingement Heat Transfer of a High

- Prandtl Number Fluid Under Conditions of Highly Varying Properties, *Journal of Heat Transfer* 121 (3) (1999) 592–597. doi:10.1115/1.2826020.
- [20] K. Bennion, G. Moreno, Convective Heat Transfer Coefficients of Automatic Transmission Fluid Jets with Implications for Electric Machine Thermal Management, in: *International Technical Conference and Exhibition on Packaging and Integration of Electronic and Photonic Microsystems (InterPACK)*, San Francisco, California, 2015.
- [21] B. Kekelia, K. Bennion, X. Feng, G. Moreno, J. E. Cousineau, S. Narumanchi, J. Tomerlin, Surface Temperature Effect on Convective Heat Transfer Coefficients for Jet Impingement Cooling of Electric Machines With Automatic Transmission Fluid, in: *ASME 2019 International Technical Conference and Exhibition on Packaging and Integration of Electronic and Photonic Microsystems*, California, 2019. doi:10.1115/IPACK2019-6457.
- [22] C. F. Ma, Q. Zheng, S. Y. Ko, Local heat transfer and recovery factor with impinging free-surface circular jets of transformer oil, *International Journal of Heat and Mass Transfer* 40 (18) (1997) 4295–4308. doi:10.1016/S0017-9310(97)00054-9.
- [23] I. Cornacchia, G. Pilla, B. Chareyron, G. Bruneaux, S. Kaiser, A. Poubreau, Development of an experimental methodology to characterize liquid cooling systems for electric motors, in: *2021 IEEE International Electric Machines Drives Conference (IEMDC)*, 2021, pp. 1–7. doi:10.1109/IEMDC47953.2021.9449572.

- [24] C. Renon, M. Fénot, M. Girault, S. Guilain, B. Assaad, An experimental study of local heat transfer using high Prandtl number liquid jets, *International Journal of Heat and Mass Transfer* 180 (2021). doi:10.1016/j.ijheatmasstransfer.2021.121727.
- [25] M. I. Najafabadi, M. Mirsalim, V. Hosseini, S. Alaviyoun, Experimental and numerical study of piston thermal management using piston cooling jet, *Journal of Mechanical Science and Technology* 28 (3) (2014) 1079–1087. doi:10.1007/s12206-013-1183-7.
- [26] G. Nasif, R. M. Barron, R. Balachandar, Heat Transfer Due to an Impinging Jet in a Confined Space, *Journal of Heat Transfer* 136 (11) (2014). doi:10.1115/1.4028242.
- [27] S. P. Kemp, J. L. Linden, Physical and chemical properties of a typical automatic transmission fluid, Tech. rep., Warrendale, PA (USA); Society of Automotive Engineers (1990).
- [28] X. Liu, Lienhard, J. H., V, J. S. Lombara, Convective Heat Transfer by Impingement of Circular Liquid Jets, *Journal of Heat Transfer* 113 (3) (1991) 571–582. doi:10.1115/1.2910604.
- [29] C. Hirt, B. Nichols, Volume of fluid (VOF) method for the dynamics of free boundaries, *Journal of Computational Physics* 39 (1) (1981) 201–225. doi:10.1016/0021-9991(81)90145-5.
- [30] S. Muzaferija, M. Peric, P. Sames, T. Schelin, A two-fluid Navier-Stokes solver to simulate water entry, in: *Proceeding of 22nd Symposium on Naval Hydrodynamics*, 1998, pp. 638–651.

- [31] X. Liu, J. H. Lienhard, The hydraulic jump in circular jet impingement and in other thin liquid films, *Experiments in Fluids* 15 (2) (1993) 108–116. doi:10.1007/BF00190950.
- [32] Y. Brechet, Z. Nédá, On the circular hydraulic jump, *American Journal of Physics* 67 (8) (1999) 723–731. doi:10.1119/1.19360.
- [33] M. T. Scholtz, O. Trass, Mass transfer in a nonuniform impinging jet: Part I. Stagnation flow-velocity and pressure distribution, *AIChE Journal* 16 (1) (1970) 82–90. doi:10.1002/aic.690160117.
- [34] X. Liu, L. A. Gabour, J. H. Lienhard, Stagnation-Point Heat Transfer During Impingement of Laminar Liquid Jets: Analysis Including Surface Tension, *Journal of Heat Transfer* 115 (1) (1993) 99–105. doi:10.1115/1.2910677.
- [35] W. M. Rohsenow, J. P. Hartnett, E. N. Ganic, *Handbook of heat transfer fundamentals*, McGraw-Hill Professional, 1985.
- [36] F. P. Incropera, D. P. DeWitt, T. L. Bergman, A. S. Lavine, et al., *Fundamentals of heat and mass transfer*, Vol. 6, Wiley New York, 1996.
- [37] D. Metzger, K. Cummings, W. Ruby, Effects of Prandtl number on heat transfer characteristics of impinging liquid jets, in: *Proceedings of 5th International Heat Transfer Conference*, Vol. 2, New York, 1974, pp. 20–24.